Rapid Communications

Spatial coherence of a strongly interacting Bose gas in the trimerized kagome lattice

Thomas H. Barter,[1] Tsz-Him Leung,[1] Masayuki Okano,[1] Maxwell Block,[1]
Norman Y. Yao,[1,2] and Dan M. Stamper-Kurn[1,2]
[1]*Department of Physics, University of California, Berkeley, California 94720, USA*
[2]*Materials Sciences Division, Lawrence Berkeley National Laboratory, Berkeley, California 94720, USA*

(Received 29 June 2019; revised manuscript received 19 December 2019; published 29 January 2020)

We produce a trimerized kagome lattice for ultracold atoms using an optical superlattice formed by overlaying triangular lattices generated with two colors of light at a 2:1 wavelength ratio. Adjusting the depth of each lattice tunes the strong intratrimer (J) and weak intertrimer (J') tunneling energies, and also the on-site interaction energy U. Two different trimerization patterns are distinguished using matter-wave diffraction. We characterize the coherence of a strongly interacting Bose gas in this lattice, observing persistent nearest-neighbor spatial coherence in the large U/J' limit, and that such coherence displays asymmetry between the strongly and the weakly coupled bonds.

DOI: 10.1103/PhysRevA.101.011601

Ultracold atoms in optical lattices provide tunable implementations of condensed-matter models. The lattices realized thus far include plaquette lattices, in which identical few-site plaquettes, with strong intraplaquette coupling, are regularly arrayed and weakly coupled to one another. Both experimentally and theoretically, such plaquette lattices allow for a controlled approach to the complexity of many-body quantum systems. At the limit of weak interplaquette coupling, the few-body states within isolated plaquettes can be precisely determined and finely controlled, enabling, for example, cold-atom demonstrations of superexchange, resonant valence states, quantum magnetism, and anyonic statistics [1–4]. These single-plaquette states serve as starting points for describing strongly correlated states that arise when interplaquette tunneling is increased.

In this Rapid Communication, we realize a lattice of triangular plaquettes known as the trimerized (or "breathing") kagome lattice (TKL). The TKL [Fig. 1(d)] is obtained by choosing one orientation of triangular plaquettes of the kagome lattice to have strong intersite tunneling (J) while plaquettes of the other orientation have weak intersite tunneling (J'). This lattice has received theoretical interest [5–7] as a route to understanding quantum antiferromagnetism in the kagome lattice. For antiferromagnetically coupled spins, the strongly coupled trimers support microscopic spin frustration. Weak intertrimer coupling then leads to robust spin-liquid ground states on macroscopic scales [5–7]. Solid-state materials with a TKL structure have been synthesized and studied in recent experiments [8,9].

Our focus here is on the behavior of strongly interacting bosons in a plaquette lattice. Specifically, we consider interacting Bose gases of ^{87}Rb atoms within a TKL with a widely tunable trimerization ratio J/J'. In the tight-binding limit, our system is modeled by the Bose-Hubbard Hamiltonian

$$H = -\sum_{\langle p,q\rangle} J_{pq}(a_p^\dagger a_q + \text{H.c.}) + \frac{U}{2}\sum_p n_p(n_p - 1), \qquad (1)$$

where $\langle p, q\rangle$ denotes summation over all pairs of neighboring lattice sites p and q, $J_{pq} = J(J')$ for strongly (weakly) coupled bonds, and n_p is the number operator for site p. Here, J and $J' > 0$. For strong trimerization ($J/J' \gg 1$) and strong interactions $U/J' \gg 1$), the TKL is predicted to support Mott insulating states in which atoms remain coherently delocalized within trimer plaquettes while intertrimer coherence is suppressed by interactions [10–12].

We present two main results. First, we develop an atom optical technique in which the momentum distribution of a superfluid trapped and transiently excited within the TKL reveals the inversion asymmetry of the TKL and distinguishes lattices of opposite trimerization.

Second, analyzing the distribution of atoms released from the lattice, we find that lattice trimerization causes the nearest-neighbor coherence to remain strong even in the deep Mott insulating limit ($U/J' \gg 1$). By an interferometric technique, we demonstrate that this spatial coherence resides almost exclusively within the trimer plaquettes.

We form the TKL by overlaying two commensurate triangular lattices, one with twice the spacing of the other [13,14]. Each triangular lattice is formed by the intersection of three focused laser beams at equal angles and lying in a single (horizontal) plane [15]. The short-wavelength (SW) lattice (lattice spacing $a_\triangle = 355$ nm) is formed by *in-plane* polarized 532-nm-wavelength light, while the long-wavelength (LW) lattice is formed by *out-of-plane* polarized 1064-nm-wavelength light. The relative position of these two lattices is stabilized interferometrically to better than 2 nm. Note that in our previous work on the regular kagome lattice, both sets of lattice beams were polarized in plane.

The unit cell of the superlattice contains four sites of the SW lattice (labeled in Fig. 1), and one site of the LW lattice. The TKL is obtained when the LW lattice site is centered between three equidistant nearest-neighbor sites of the SW lattice, which now form the trimer of the trimerized lattice. For example, two trimerizations, with opposite spatial inversion

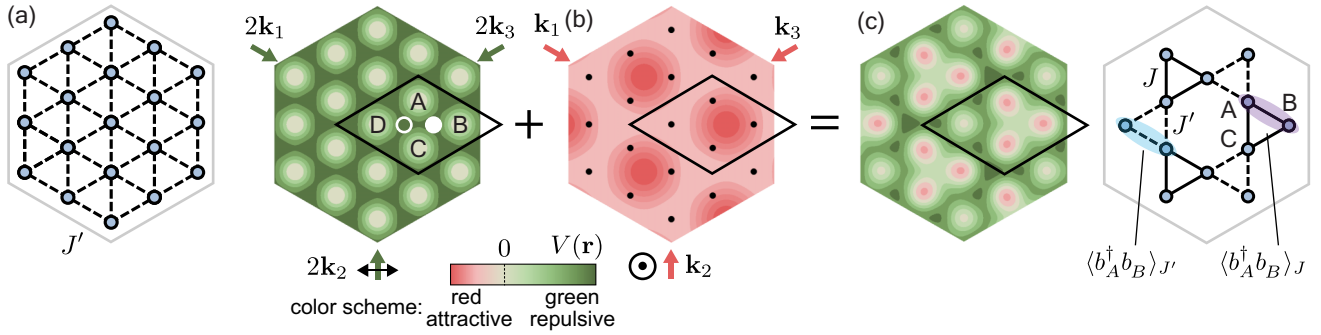

FIG. 1. Construction of the optical TKL. (a) A SW triangular lattice of spacing $a_\triangle = 355$ nm is formed by in-plane polarized 532-nm-wavelength light. Sites of a 2×2 unit cell are labeled A–D. Two locations of the LW lattice site, corresponding to right and left trimerizations, are shown as solid and open white dots, respectively. (b) A LW triangular lattice of spacing $2a_\triangle$ is formed by out-of-plane polarized 1064-nm-wavelength light. Black dots indicate sites of the SW lattice. (c) Combined superlattice potential for the right TKL. (d) Tight-binding model of the TKL, with strong intratrimer tunneling J and weak intertrimer tunneling J'.

asymmetry, are obtained by centering the LW lattice sites at locations shown in Fig. 1(a).

The LW lattice has three effects on the overall superlattice. First, the energies of the three sites in the trimer are lowered relative to the fourth one roughly by $\Delta V \approx \frac{1}{2}V_{\mathrm{LW}}$, where V_{LW} is the depth of the LW lattice potential. When ΔV is sufficiently high, the fourth site is unoccupied and a kagome structure is realized. Second, the tunneling barrier between sites within a trimer is decreased, while the barrier between trimers is increased, leading to the trimerization of tunneling energies ($J > J'$). Third, the combined lattice "breathes," with the spacing between trimer sites (a) decreasing, and the nearest-neighbor spacing between trimers (a') increasing.

We visualize the spatial asymmetry of the TKL through the coherent diffraction of a superfluid from the lattice. For this, we prepare nearly pure Bose-Einstein condensates of 5×10^4 ^{87}Rb atoms in a hybrid optical and magnetic harmonic trap, with trap frequencies $(\omega_x, \omega_y, \omega_z) = 2\pi \times (40, 70, 80)$ Hz, with $\mathbf{z}$ being the vertical axis. The atoms are loaded into the superlattice by simultaneously increasing depths of the SW and LW lattices to $V_{\mathrm{SW}}/h = 45$ kHz and $V_{\mathrm{LW}}/h = 15$ kHz by an exponential ramp [16]. The relative position of the two lattices is adjusted to produce C_6 symmetric diffraction patterns of gases released from the lattice. The gas remains only loosely confined along the transverse (vertical) direction.

The momentum space distribution of this superfluid in equilibrium, shown in Fig. 2(a), does not manifest the broken inversion symmetry and reduced rotational symmetry of the lattice, since the superfluid order parameter has a uniform phase. To fully characterize the lattice, we imprint complex phases onto the superfluid wave function through transient dynamics. After allowing the superfluid 20 ms to equilibrate in the TKL, we suddenly extinguish the SW lattice potential and allow the atoms to evolve for a variable time $0 < \tau < 150$ μs in the remaining LW lattice. We then switch off all potentials, allow the atoms to expand freely for 20 ms, and image their spatial distribution by absorption imaging.

The two lattice trimerizations lead to strong but opposite inversion-asymmetric diffraction patterns. We focus on the first-order diffraction peaks, occurring at reciprocal lattice vectors $\mathbf{G}_1 = \mathbf{k}_2 - \mathbf{k}_3$ and its cyclic permutations, where $\mathbf{k}_i$ are wave vectors of the LW lattice beams. We observe

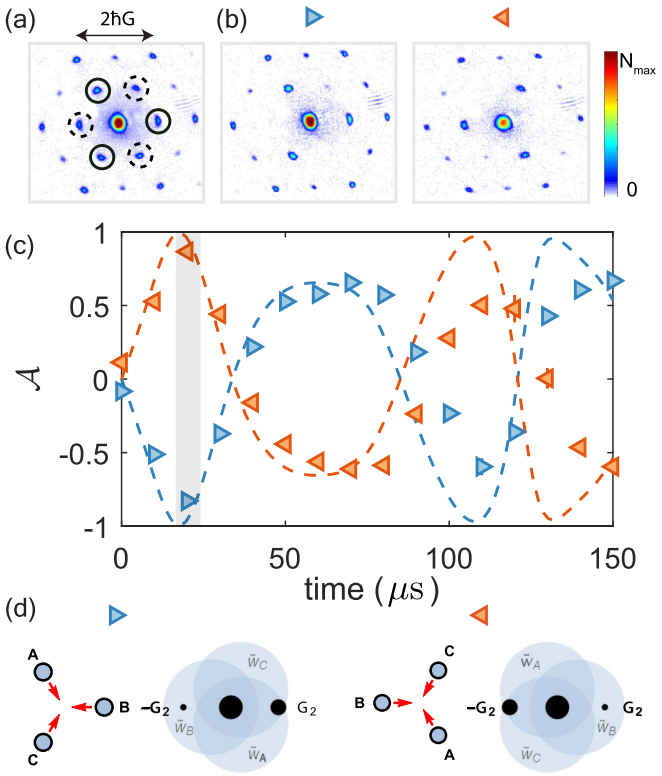

FIG. 2. Trimerization-dependent momentum space asymmetry. (a) Momentum distribution of a superfluid within the TKL shows no asymmetry between $\mathbf{G}_i$ (solid circles) and $-\mathbf{G}_i$ (dashed circles). (b) Strong inversion asymmetry is seen after $\tau = 20$ μs of evolution in the LW lattice potential, with opposite sign for right (blue triangle) and left (red triangle) trimerizations. (c) Oscillations of the asymmetry parameter $\mathcal{A}$ vs τ occur with opposite sign for the right and left trimerizations. Data points represent the average over 2–7 iterations. The dashed line is calculated by noninteracting band theory. Error bars are standard errors of mean. (d) Explanation of the population asymmetry at early τ. Red arrows show the direction of acceleration experienced by the Wannier functions at sites A, B, and C for the two different trimerizations. The resultant impulses displace the Wannier functions (contours shown as blue circles) in momentum space. Imbalance between $P_{\mathbf{G}_2}$ and $P_{-\mathbf{G}_2}$ results from the interference of displaced Wannier functions.

the diffracted populations $P_{\mathbf{G}_i}$ at wave vectors $\mathbf{G}_i$ to differ from those at $-\mathbf{G}_i$ [Fig. 2(b)]. Quantifying the asymmetry by the parameter $\mathcal{A} = [\sum_i (P_{\mathbf{G}_i} - P_{-\mathbf{G}_i})]/[\sum_i (P_{\mathbf{G}_i} + P_{-\mathbf{G}_i})]$ [17], we observe equal and opposite oscillations of $\mathcal{A}$ as a function of τ [Fig. 2(c)], distinguishing the opposite inversion asymmetry of the two trimerization patterns. The data match noninteracting band theory well for $0 < \tau < 80\ \mu$s. We attribute the discrepancy between theory and data at later times ($\tau > 80\ \mu$s) to dephasing caused by interactions.

To realize the strongly interacting Bose-Hubbard Hamiltonian, we introduce an additional one-dimensional optical lattice, formed by a retroreflected 1064-nm-wavelength light beam propagating along **z**. This lattice, with a depth $V_\perp/h =$ 50 kHz, divides the gas into about 40 layers, each with trap frequencies $(\omega_x, \omega_y, \omega_z) = 2\pi \times (61, 61, 22 \times 10^3)$ Hz. As the tunneling time between layers of 400 ms is slower than the timescale of the experiment, the system can be considered as an ensemble of isolated, two-dimensional systems [18].

The superlattice is ramped up as above, but to variable final lattice depths. The ramp is adiabatic with respect to U, J, J', and the band gap. During the ramp, an additional single-pass, vertically propagating, 1064-nm-wavelength light beam provides confinement and maintains a constant Thomas-Fermi radius in each layer.

After being held on for 40 ms, all potentials are simultaneously switched off, and the gas is allowed to expand for 16 ms before being imaged. The observed distribution approximates the momentum distribution of the lattice-trapped gas [19].

In the tight-binding limit, the momentum distribution of a lattice-trapped Bose gas is given by

$$n(\mathbf{k}) = w_p^*(\mathbf{k}) w_q(\mathbf{k}) \sum_{p,q}^{\text{all}} e^{i\mathbf{k}\cdot(\mathbf{r}_p - \mathbf{r}_q)} \langle b_p^\dagger b_q \rangle, \tag{2}$$

where $\langle b_p^\dagger b_q \rangle$ is the coherence between site p and q, with $\mathbf{r}_p$ being the position and $w_p(\mathbf{k})$ the Fourier-space Wannier function at site p, and the summation runs over all lattice sites [19].

For large U/J', $\langle b_p^\dagger b_q \rangle$ vanishes rapidly for distant p and q. To leading order we consider only the nearest-neighbor (NN) terms, so that the momentum distribution is approximated as [15,20,21]

$$\frac{n(\mathbf{k})}{N} \simeq |\tilde{w}(\mathbf{k})|^2 \left(1 + \sum_{p<q}^{\text{cell}} \text{Re}\left[\zeta_{pq} e^{i\mathbf{k}\cdot\mathbf{a}_{pq}} + \zeta'_{pq} e^{i\mathbf{k}\cdot\mathbf{a}'_{pq}}\right]\right), \tag{3}$$

where N is the total atom number, ν is the average filling per site, and the indices p and q now run over sites in the unit cell. Here, $\mathbf{a}_{pq} = \mathbf{r}_p - \mathbf{r}_q$ is the (intratrimer) distance vector between sites p and q, and $\zeta_{pq} = \frac{2}{\nu}\langle b_p^\dagger b_q \rangle$, where ν is the filling per site, quantifies their mutual coherence, evaluated over an intratrimer bond. Similarly, a', ζ' are evaluated over an intertrimer bond. For simplicity, we assume an identical cylindrically symmetric Wannier function $\tilde{w}(\mathbf{k})$ at each site, neglecting small site-dependent ellipticity at the settings of our experiment.

We measure spatial coherence in the trimerized kagome lattice at two fixed intratrimer interaction strengths, $U/J =$ 5.9 and 19 [22]. As we increase U/J', the sharply peaked momentum distribution of the superfluid gives way to a broad momentum distribution, indicating the loss of long-range phase coherence. However, even in the strongly interacting regime, the momentum distribution still shows modulations that indicate the persistence of short-ranged spatial coherence.

We quantify the NN coherence by fitting the observed distribution with the function

$$\frac{n(\mathbf{k})}{N} = |\tilde{w}(\mathbf{k})|^2 \left(1 + \sum_{p<q}^{\text{cell}} [\alpha_{pq} \cos(\mathbf{k}\cdot\mathbf{a}_{pq}) + \beta_{pq} \sin(\mathbf{k}\cdot\mathbf{a}_{pq})]\right). \tag{4}$$

Compared with Eq. (3), this expression is simplified by including only one momentum-space periodicity along each lattice direction. This simplification is justified both for weak trimerization, where the lengths a and a' are nearly equal, and also for strong trimerization, where (as we show) the intratrimer coherence dominates over the intertrimer coherence. As such, we identify $\alpha_{\text{AB}} \simeq \text{Re}(\zeta_{\text{AB}} + \zeta'_{\text{BA}})$ and $\beta_{\text{AB}} \simeq \text{Im}(\zeta_{\text{AB}} + \zeta'_{\text{BA}})$, and similar for other bond directions. Both the Gaussian width of $\tilde{w}(\mathbf{k})$ and also the bond lengths a_{pq} are used as fitting parameters and extracted from the images.

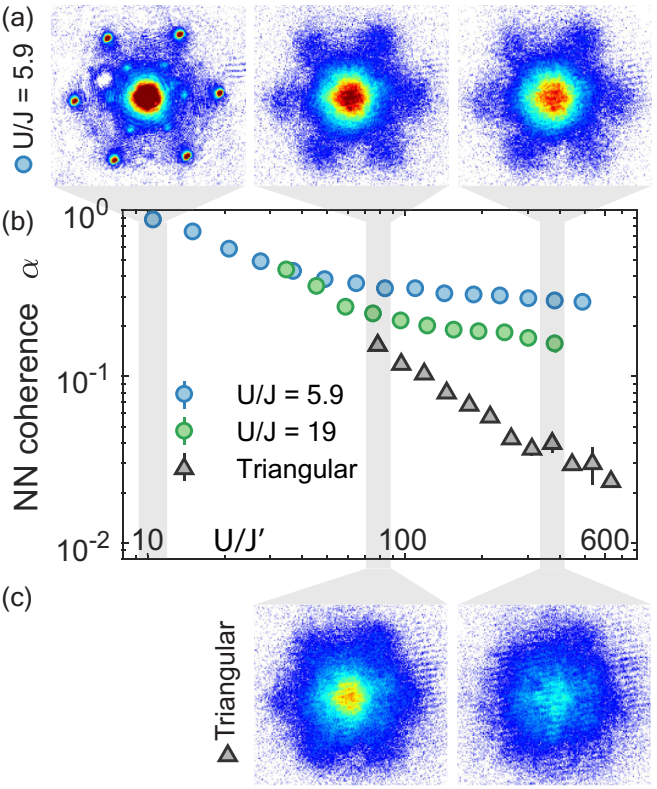

FIG. 3. Time-of-flight images of strongly interacting atoms released from either the (a) TKL or (c) triangular lattice. As U/J' is increased at constant U/J, sharp diffraction peaks are lost, leaving a broad sixfold symmetric modulation. This modulation persists at large U/J' in the TKL, but disappears in the triangular lattice. The color scale is the same as that in Fig. 2. (b) Extracted NN coherence α for the trimerized kagome (blue, green circles) and triangular lattice (triangles). Data points are the average of 3–9 measurements. Error bars are standard errors of mean.

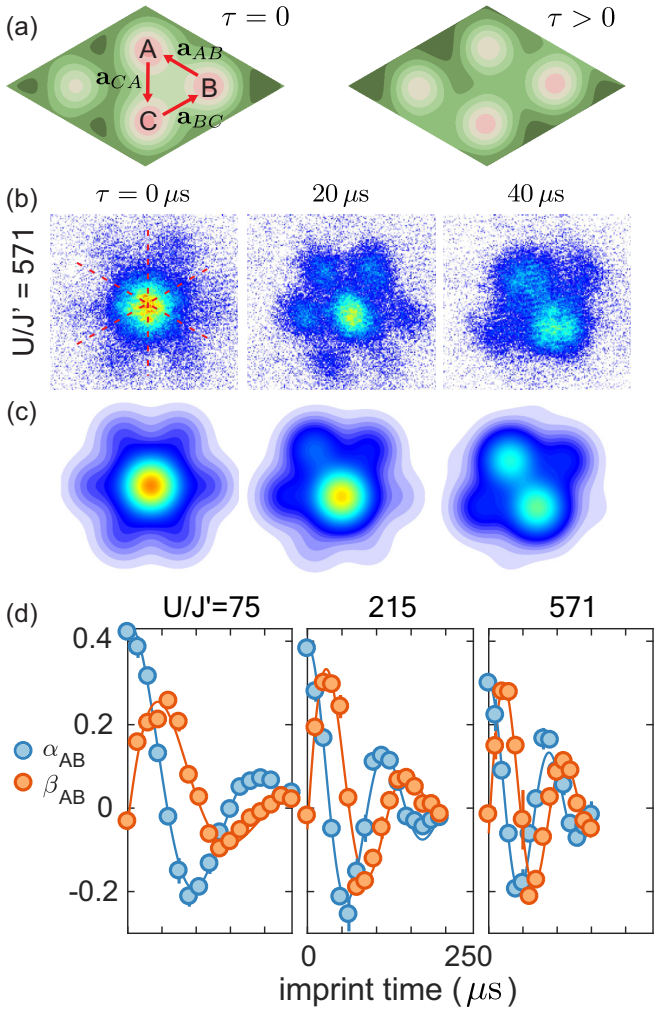

FIG. 4. Revealing coherence asymmetry via phase imprinting. (a) Change in the TKL potential when one LW lattice beam is switched off. Site A is detuned from sites B and C by ΔV. (b) The phase imprint from applying this energy offset for variable τ causes the initially symmetric momentum distribution ($\tau = 0$) to evolve. Dashed lines have the same directions as the lattice distance vectors and indicate the directions of modulation. The color scale is the same as that in Fig. 2. (c) Similar distributions are calculated for a superposition of three identical Gaussian wave functions at the sites of a trimer, with a complex phase applied at one site. The width of the Gaussian function and the visibility of interference are based on experimental parameters. (d) Coherence functions α_{AB} and β_{AB} obtained from fitting Eq. (4) to the observed momentum distributions oscillate out of phase. The equal amplitudes of oscillation for strong trimerization ($U/J' = 215$ and 571) show that NN coherence resides nearly exclusively on the strongly coupled bonds. Data points are averages of 2–3 measurements. Error bars are standard errors of mean.

For the data of Fig. 3, we set $\beta_{pq} = 0$ since the coherence in this case is expected to be real valued. A single value for the NN coherence function α is taken as the average of α_{pq} along the three bond directions [23].

Our measurements on the TKL are benchmarked by similar measurements performed on atoms in the primitive triangular lattice. For this, we prepare the gas as before, with the exception that the LW lattice light is left off.

The fitted NN coherences demonstrate the influence of lattice trimerization. At low U/J', in the superfluid regime, the NN coherences of the triangular and TKL are similar. At large U/J', there is a stark difference. In the triangular lattice, the NN coherence tends to zero in the Mott insulating limit, scaling as $\alpha \propto (U/J)^{-0.87(9)}$, which is roughly consistent with a perturbative treatment of a Mott insulator with uniform tunneling energies [15,20,21]. In contrast, for the TKL, NN coherence remains large due to persistent tunneling within trimers. We also observe that α is smaller for larger U/J, showing the effect of interactions to suppress coherence in a few-site system.

The simultaneous lack of long-range coherence and persistence of nearest-neighbor coherence implies that spatial coherence in the TKL is spatially asymmetric, with large differences between $\langle b_p^\dagger b_q \rangle_J$ and $\langle b_p^\dagger b_q \rangle_{J'}$. We confirm this fact by an interferometric measurement, in which we imprint a site-specific phase on the spatial coherence [24]. For this, we turn off one beam of the LW lattice for a brief time τ, raising the energy of one site in each trimer (A) above the energy of the other two sites (B and C) by $\Delta V \simeq 0.2 V_{LW}$. This energy offset causes the coherence functions to become complex, evolving as $\zeta_{AB}(\tau) = e^{i\phi}\zeta_{AB}(0)$ and $\zeta'_{AB}(\tau) = e^{-i\phi}\zeta'_{AB}(0)$, and similar for ζ_{AC} and ζ'_{AC}, with $\phi = \Delta V\,\tau/\hbar$.

This phase imprint has a pronounced effect on the momentum distribution (Fig. 4). In the limit that NN coherence remains only on the intratrimer bonds, we expect $\alpha_{AB} \propto \cos(\phi)$ and $\beta_{AB} \propto \sin(\phi)$ to oscillate out of phase and with equal amplitude with τ. Fitting the observed momentum distribution using Eq. (4) while allowing for nonzero β_{pq} and time-varying spacings a_{pq}, we observe such equal amplitude oscillations

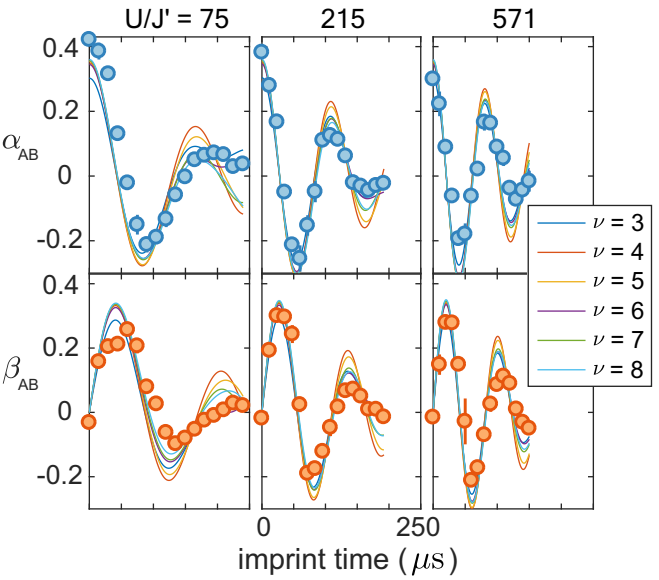

FIG. 5. Comparison of the nearest neighbor coherence data (circles) to an exact solution of the three-site Bose-Hubbard model (solid lines) for the phase imprint experiment. Theory lines have been uniformly scaled by 2/3 in the y axis. The multiple theory lines correspond to different particle numbers ν per trimer.

for the case of strong interactions and strong trimerization, demonstrating that, for these settings, NN coherence resides nearly exclusively on the intratrimer bonds. In the case of weaker trimerization and closer to the superfluid regime, we still observe oscillations in β_{AC}, but with diminished amplitude with respect to those in α_{AC}. This observation demonstrates that, while NN coherences in this case are still stronger on the intratrimer bonds, there exists a discernible coherence also on the intertrimer bonds.

The temporal oscillations of $\alpha(\tau)$ $[\beta(\tau)]$ are not purely cosinusoidal (sinusoidal), and appear to decay in time. To model this behavior, we study the dynamics of a three-site Bose-Hubbard model. The ground state is calculated and projected onto the eigenstates of a new Hamiltonian $H_{\Delta V}$ that accounts for an energy offset ΔV_A on site A. We do not account for changes to U and J in the new potential. We also neglect the transport of atoms into nearby plaquettes or onto the now-accessible D sites of the lattice, assuming that such transport affects the experimental system only over longer timescales than probed by our measurements.

As shown in Fig. 5, we find good agreement between the measured coherences α_{AB} and β_{AB} and those calculated from this model. The decay of the oscillations in α_{AB} and β_{AB} is explained as a beating between several frequencies in the few-body spectrum of $H_{\Delta V}$. Note that we have scaled the theoretically determined coherence by a factor of $2/3$ to obtain a good agreement, presumably to account for effects of nonzero temperature.

Our present work is performed at high filling, reaching $\nu \simeq 8/3$ atoms per site (8 atoms per trimer) at the center of the gas. Reaching filling factors below $\nu = 1$ would allow for studies of the predicted fractional (per site) Mott insulating state [11]. Future experiments may identify few-body eigenstates within single trimers by precise spectroscopy. These eigenstates include circulating states, to which atoms can be driven to realize models for orbital magnetism [25]. Alternately, two-state fermions within the TKL at half filling can simulate the spin-$1/2$ Heisenberg antiferromagnet, which is expected to have a spin-liquid ground state [25–27].

We thank Y. M. Tso for experimental assistance. This work was supported by the NSF, and by the AFOSR and ARO through the MURI program (Grants No. FA9550-14-1-0035 and No. W911NF-17-1-0323, respectively).

[1] S. Trotzky, P. Cheinet, S. Folling, M. Feld, U. Schnorrberger, A. M. Rey, A. Polkovnikov, E. A. Demler, M. D. Lukin, and I. Bloch, Science **319**, 295 (2008).
[2] S. Nascimbène, Y. A. Chen, M. Atala, M. Aidelsburger, S. Trotzky, B. Paredes, and I. Bloch, Phys. Rev. Lett. **108**, 205301 (2012).
[3] D. Greif, T. Uehlinger, G. Jotzu, L. Tarruell, and T. Esslinger, Science **340**, 1307 (2013).
[4] H.-N. Dai, B. Yang, A. Reingruber, H. Sun, X.-F. Xu, Y.-A. Chen, Z.-S. Yuan, and J.-W. Pan, Nat. Phys. **13**, 1195 (2017).
[5] V. Subrahmanyam, Phys. Rev. B **52**, 1133 (1995).
[6] F. Mila, Phys. Rev. Lett. **81**, 2356 (1998).
[7] M. Mambrini and F. Mila, Eur. Phys. J. B **17**, 651 (2000).
[8] J.-C. Orain, B. Bernu, P. Mendels, L. Clark, F. H. Aidoudi, P. Lightfoot, R. E. Morris, and F. Bert, Phys. Rev. Lett. **118**, 237203 (2017).
[9] F. H. Aidoudi, D. W. Aldous, R. J. Goff, A. M. Z. Slawin, J. P. Attfield, R. E. Morris, and P. Lightfoot, Nat. Chem. **3**, 801 (2011).
[10] P. Buonsante, V. Penna, and A. Vezzani, Phys. Rev. A **72**, 031602(R) (2005).
[11] O. Jürgensen and D.-S. Lühmann, New J. Phys. **16**, 093023 (2014).
[12] Q.-H. Chen, P. Li, and H. Su, J. Phys: Condens. Matter **28**, 256001 (2016).
[13] G.-B. Jo, J. Guzman, C. K. Thomas, P. Hosur, A. Vishwanath, and D. M. Stamper-Kurn, Phys. Rev. Lett. **108**, 045305 (2012).
[14] C. K. Thomas, T. H. Barter, T.-H. Leung, M. Okano, G.-B. Jo, J. Guzman, I. Kimchi, A. Vishwanath, and D. M. Stamper-Kurn, Phys. Rev. Lett. **119**, 100402 (2017).
[15] C. Becker, P. Soltan-Panahi, J. Kronjager, S. Doscher, K. Bongs, and K. Sengstock, New J. Phys. **12**, 065025 (2010).
[16] The SW and LW lattices are initially turned on at $V_{SW}/h = 2$ kHz and $V_{LW}/h = 1$ kHz respectively to initiate position stabilization. After 20 ms, the lattice depths are increased exponentially in time, with a time constant of $\tau = 35$ ms for the SW lattice, while that for the LW lattice varies between 32 and 58 ms depending on the final depth such that the two ramps always finish at the same time.
[17] C. K. Thomas, T. H. Barter, T.-H. Leung, S. Daiss, and D. M. Stamper-Kurn, Phys. Rev. A **93**, 063613 (2016).
[18] D. S. Petrov, M. Holzmann, and G. V. Shlyapnikov, Phys. Rev. Lett. **84**, 2551 (2000).
[19] F. Gerbier, S. Trotzky, S. Folling, U. Schnorrberger, J. D. Thompson, A. Widera, I. Bloch, L. Pollet, M. Troyer, B. Capogrosso-Sansone, N. V. Prokof'ev, and B. V. Svistunov, Phys. Rev. Lett. **101**, 155303 (2008).
[20] F. Gerbier, A. Widera, S. Folling, O. Mandel, T. Gericke, and I. Bloch, Phys. Rev. Lett. **95**, 050404 (2005).
[21] I. B. Spielman, W. D. Phillips, and J. V. Porto, Phys. Rev. Lett. **98**, 080404 (2007).
[22] Values of U, J, and J' for each setting of V_{SW}, V_{LW}, and $V_{\perp}$ were calculated following Ref. [28].
[23] Close to the superfluid regime, finer modulations in momentum space, indicating coherence beyond the nearest neighbor, are also seen. Through numerical simulation, we verify that these additional modulations do not affect the fits by which the NN coherence is extracted.
[24] S. Taie, H. Ozawa, T. Ichinose, T. Nishio, S. Nakajima, and Y. Takahashi, Sci. Adv. **1**, e1500854 (2015).
[25] B. Damski, H. U. Everts, A. Honecker, H. Fehrmann, L. Santos, and M. Lewenstein, Phys. Rev. Lett. **95**, 060403 (2005).
[26] L. Santos, M. A. Baranov, J. I. Cirac, H.-U. Everts, H. Fehrmann, and M. Lewenstein, Phys. Rev. Lett. **93**, 030601 (2004).
[27] B. Damski, H. Fehrmann, H. U. Everts, M. Baranov, L. Santos, and M. Lewenstein, Phys. Rev. A **72**, 053612 (2005).
[28] R. Walters, G. Cotugno, T. H. Johnson, S. R. Clark, and D. Jaksch, Phys. Rev. A **87**, 043613 (2013).